

## Tribocorrosion damage of a Jethete M152 type stainless steel

S.C. Wang<sup>a,\*</sup>, S. Quinn<sup>b</sup>, M.J. Starink<sup>a</sup>, R.J.K. Wood<sup>a,b</sup> and J.A. Wharton<sup>a</sup>

<sup>a</sup> Materials Research Group, School of Engineering Sciences; University of Southampton, Southampton, SO17 1BJ, United Kingdom

<sup>b</sup> Research Institute for Industry (RII), School of Engineering Sciences; University of Southampton, Southampton, SO17 1BJ, United Kingdom

### Abstract

An insert made from Jethete M152 type stainless steel (Fe-12Cr) was used for moulding a polymer product, but failed in-service due to the formation of oxidation/corrosion products. The investigation of the failure mechanism has been carried out using scanning and transmission electron microscopy (SEM and TEM). A high density of fine precipitates, 50-200 nm in size, were observed in the etched samples by SEM. TEM analysis combined with convergent beam electron diffraction (CBED) showed that the precipitates are  $(\text{Cr,Fe,Mo})_{23}\text{C}_6$  carbides which possess  $\text{Fm}\bar{3}\text{m}$  space group with a lattice parameter of  $1.07\pm 0.03$  nm. The formation mechanisms of the precipitates were studied by investigating a range of heat treatments.

**Keywords:** Precipitate; Oxidation; Jethete M152 alloy; Tribocorrosion.

\* Corresponding author. Tel: +44 23 8059 4638  
E-mail address: [wangs@soton.ac.uk](mailto:wangs@soton.ac.uk) (S.C. Wang)

### 1. Introduction

Fe-12Cr (12 wt.% Cr) steel alloys belong to the class of martensitic stainless steels and have a combination of properties which include good ductility at high strength levels, uniform properties throughout thick sections and favourable strength at temperatures up to about 480°C [1]. Stainless steels are iron-based alloys that contain a minimum of approximately 11 wt.% Cr, the amount needed to improve the corrosion performance. Martensitic stainless steels possess a body-centred tetragonal (bct) crystal structure after quenching from an austenite phase (face-centred cubic structure) at high temperature. The chromium content is generally in the range of 10.5 to 18.0 wt.%, and carbon content may exceed 1.2 wt.%. The chromium and carbon contents are carefully balanced to ensure a martensitic structure after hardening. Jethete M152 is a member of the Fe-12Cr family of alloys, with the addition of Ni and Mo. It features outstanding fracture toughness and good oxidation resistance up to approximately 425°C, as well as the properties common to other Fe-12Cr alloys, noted above. These features, together with its favourable coefficient of expansion, make the alloy attractive for use for steam turbine components and compressor parts in gas turbine applications.

In this application Jethete M152 was used for a production tool, as a mould for manufacture of a polymer product. The operating conditions are a maximum temperature of approximately 230°C although the tool remains much cooler (30 to 40°C) and a pressure of approximately 1000 bar in an oxygen containing environment. Each tool is subjected to approximately 10,000 cycles per day. Jethete M152 stainless steel was chosen for this application due to its corrosion resistance, however, in-service failures occurred and were linked to the formation of corrosion/oxidation products

covering part of the surface. The purpose of this paper is to determine the possible failure mechanism, and to identify and analyse any deleterious phases present in the alloy.

## 2. Experimental procedures

Jethete M152 stainless steel was prepared using the vacuum induction melting (VIM) and vacuum arc remelting (VAR) processes, which results in a stainless steel of higher purity, lower non-metallic inclusion content and fine grains. Inserts were fabricated after the alloys were softened at 690°C for 6h. The inserts were solution treated at 1050°C for 1h, oil quenched, and tempered at 560°C for 3h followed by air cooling. The chemical composition of inserts is shown in Table 1.

Table 1. The chemical composition of the inserts (wt.%)

| C    | Cr   | Ni   | Mo   | Mn   | V    | Si   | N     | P     | S     | Fe        |
|------|------|------|------|------|------|------|-------|-------|-------|-----------|
| 0.12 | 11.4 | 2.72 | 1.64 | 0.58 | 0.31 | 0.23 | 0.024 | 0.023 | 0.005 | remainder |

Samples of the failed and virgin (no prior operational service) insert components were investigated. To reveal the microstructure, inserts were sectioned, mounted in bakelite and wet ground on 120, 600, 1200 and 4000 grit SiC papers successively, and then etched for 30 sec in a solution of 80 cm<sup>3</sup> HCl, 5 cm<sup>3</sup> HNO<sub>3</sub>, 1 g CuCl<sub>2</sub> and 20 cm<sup>3</sup> distilled water. Microstructures were examined using a JEOL JSM-6500 FEG-SEM (field emission gun-scanning electron microscope), operating at 15 kV, with an Oxford Instruments energy dispersive X-ray spectrometry (EDS) analysis system. Discs of 3 mm in diameter were punched out from the slices of the specimens for Transmission Electron Microscopy (TEM) analysis, and then electropolished using a solution of HNO<sub>3</sub> and methanol (1:3 in volume). The TEM foils were examined using a JEOL 3010 microscope operating at 300 kV.

## 3. Results

### 3.1 Optical observation of the damaged edges of inserts

Fig. 1 shows a macrograph of an insert which failed in-service. There are several scratches from top to bottom, which were formed during assembly of the insert into the sleeve component. Heavy stains (dark red by visual appearance) were associated with these scratches, although some stains occur on the insert surface where no scratches exist.

### 3.2 SEM analysis of the oxidation/corrosion products

Fig. 2a shows a secondary electron image (SEI) of one corrosion area on the insert, which corresponds to area 1 in Fig. 1. It appears that corrosion products are occurring preferentially in the scratches. Oxidation is present around the vast majority of the circumference of the outer rim of the insert and it varies in length along the insert at different circumferential positions. However, there was no evidence that oxidation/corrosion occurred preferably at grain boundaries. The backscatter electron image (BEI) at higher magnification (Fig. 2b) shows two kinds of morphologies: one is relatively bright (area A) and covering a substantial part of the surface, and the other is debris-like (area B). EDS confirms that the chemical composition at both areas have high oxygen contents, and the ratios of (Fe + Cr) / O are about 0.77 and 0.66 respectively, see Table 2. Such oxidation products are similar to those found on Nd-Fe-B alloys [2], where a Fe<sub>3</sub>O<sub>4</sub> (magnetite) will form first and then transform into Fe<sub>2</sub>O<sub>3</sub> (hematite) under further oxidation (including a small amount of Cr<sub>2</sub>O<sub>3</sub>). Therefore, it can be concluded that serious oxidation occurs in the scratches formed during operation.

Table 2. The compositions of two typical oxidation / corrosion products (at.%)

| Area | O     | Si   | Cr   | Fe    | Ni   | Mo   | (Fe+Cr)/O | Products (ratio)  |
|------|-------|------|------|-------|------|------|-----------|---|
| A    | 54.71 | 0.67 | 5.84 | 36.21 | 2.07 | 0.49 | 0.77      | Fe <sub>3</sub> O <sub>4</sub> +Cr <sub>2</sub> O <sub>3</sub> (~6:1) |
| B    | 58.40 | 2.00 | 3.95 | 34.76 | 0.16 | 0.73 | 0.66      | Fe <sub>2</sub> O <sub>3</sub> +Cr <sub>2</sub> O <sub>3</sub> (~9:1) |

It was also noted that some oxidation products occur on the insert surface, that are not associated with scratches, as shown in area 2 of Fig. 1. The corresponding BEI micrograph is shown in Fig. 3. The areas of dark colour were determined to be oxidation products of Fe<sub>2</sub>O<sub>3</sub>. The black particles were carbon rich, which was assumed to be due to contamination from polymer products manufactured at high temperature.

### 3.3 SEM observation of the etched samples / TEM analysis

After etching, distinct particles in the range of 50–200 nm are visible in an insert which failed during service, as shown in Fig. 4(a). EDS in SEM shows that the particles are chromium enriched. To help determine when this chromium enrichment occurs, an as-manufactured insert was also investigated. A transverse section was prepared from this virgin material. The high magnification micrograph in SEM (Fig. 4b) shows that there are chromium particles in the same size range as the virgin material. This indicates that the precipitates are introduced in the heat treatments during production of the raw material.

As X-rays activate an area (0.5–1.0 μm in steel bombarded at 15 kV) that is much larger than the dimension of the precipitates (50–200 nm), the composition of the precipitates cannot be determined accurately in SEM. The structure of these small precipitates is also difficult to identify by electron backscattering diffraction (EBSD) in SEM. TEM has therefore been utilised to analyse the structure information and the chemical composition of the precipitates. Fig. 5(a) shows two precipitates in bright field mode. The EDS spectrum in Fig. 5(b) confirms these particles are Cr rich, and also significant amounts of C, Mo, Fe and some V are detected. Table 3 shows the composition from EDS for one precipitate as well as the matrix. The composition of C is detected in variable from 13 to 20 at.%. Figs. 5(c-e) show three selected area diffraction (SAD) patterns of the precipitate. These are fully consistent with [001], [112] and [111] zones in a face-centred cubic (fcc) structure. No forbidden reflection was observed. The corresponding lattice parameter (*a*) was measured to be 1.07 ± 0.03 nm (using the Al matrix as a reference).

Table 3. Chemical compositions of the unknown fcc phase determined from EDS (at. %)

| Phase         | C    | Si  | V   | Cr   | Mn  | Fe   | Ni  | Mo  |
|---------------|------|-----|-----|------|-----|------|-----|-----|
| Precipitate 1 | 20.2 | 0.1 | 1.6 | 51.6 | 0.4 | 19.0 | 0.7 | 6.4 |
| Matrix        | 3.8  | 0.6 | 0.2 | 12.7 | 0.4 | 78.6 | 2.6 | 1.1 |

In three dimensions, the space groups specify the total symmetry of the arrangement of atoms in a crystal. The 230 Space Groups result from the systematic combination of the 14 Bravais lattices with the 32 Crystallographic Point Groups and the screw axis/translation element. The diffraction micrographs in Figs. 5(c-e) evidence that the precipitates has fcc structure (one of 14 Bravais lattices) without any screw axis / translation element (no forbidden reflections). The point group of the precipitate is determined using convergent beam electron diffraction (CBED), which can distinguish all 32 possible point groups unambiguously even for the present very small precipitate. There are two specific kinds of symmetry to look at in CBED patterns: Bright-field (BF) symmetry and Whole-pattern (WP) symmetry. The BF symmetry refers to the symmetry of high-order-Laue-zone (HOLZ) lines presented in the 000 disk. The WP symmetry is the symmetry of the HOLZ

lines and zero-order-Laue-zone (ZOLZ) Kikuchi lines in the pattern as a whole. From the BF and WP symmetries of CBED patterns obtained from several prominent zone axes, it is possible to find one of 31 diffraction groups, and then the possible point group, based on Steeds and co-worker's work [3,4]. A [001] zone CBED pattern is shown in Fig. 6a. According to the principle of HOLZ line formation [5], HOLZ lines in BF disc correspond to those in higher order Laue ring, therefore the latter's symmetry refers to the BF symmetry. Kikuchi lines and bands show the ZOLZ symmetry. Consequently the symmetries of both Kikuchi and HOLZ lines represent the WP symmetry. As indicated by the arrow and  $m$  (mirror) in Fig. 6a, the BF symmetry and the WP symmetry both show 4-fold axis and mirror, i.e.  $4mm$ . The [111] zone CBED pattern is shown in Fig. 6b. Similarly, the symmetries of both BF and WP are  $3m$  because the HOLZ ring and the array of HOLZ-deficient Kikuchi lines show threefold symmetry with one mirror plane reproduced every  $120^\circ$ . The results are summarised in columns 2 and 3 of Table 4. Further possible diffraction groups and point groups can be deduced according to the work of Refs [3,4] as shown in Table 3. The point group for the precipitate, therefore, is  $m\bar{3}m$  as it satisfies the symmetries of both [001] and [111] zones. Combined with the Bravais lattices, it is possible to identify the space group of the crystal of  $Fm\bar{3}m$ .

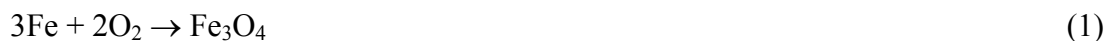
Table 4. Determination of CBED symmetries and possible point groups

| Zone  | BF symmetry | WP symmetry | Possible diffraction groups | Possible point groups                          |
|-------|-------------|-------------|-----------------------------|--|
| [001] | $4mm$       | $4mm$       | $4mm$ or $4mm1_R$           | $4mm$ , $4/mmm$ or $m\bar{3}m$                 |
| [111] | $3m$        | $3m$        | $3m$ or $6_{Rmm_R}$         | $3m$ , $\bar{3}m$ , $4\bar{3}m$ or $m\bar{3}m$ |

## 4. Discussion

### 4.1 Thermodynamics of oxidation

When a metal is exposed to an oxidising environment at elevated temperatures, such as an environment that contains molecular oxygen ( $O_2$ ), degradation can occur by direct action of the gas, without the need for the presence of a liquid electrolyte. This type of degradation/corrosion is often referred to as tarnishing, high-temperature oxidation, or scaling. The rate of attack increases substantially with temperature [6,7]. The EDS analysis, in Section 3.2, indicated that both  $Fe_3O_4$  and  $Fe_2O_3$  oxides were present in the oxidation products with small amounts of  $Cr_2O_3$ . The working temperature during operation was approximately  $200^\circ C$ . According to the  $\Delta G^\circ$ -T oxide formation ("Ellingham-Richardson") diagram [8], the formation of  $Fe_3O_4 / Fe_2O_3$  oxides is possible, as both reactions are exothermic:



$$\Delta G^\circ_{200^\circ C} = -210 \text{ kJ}$$



$$\Delta G^\circ_{200^\circ C} = -310 \text{ kJ}$$

In general, for oxidation-resistant Fe-Cr steels to be fully effective they must contain sufficient chromium to form a thin protective oxide layer, consisting largely of  $Cr_2O_3$ , which acts as a barrier between the oxygen and the underlying metal. If the proportion of chromium is less than that required to provide complete protection, the chromium can also diffuse into the iron oxides formed. Low-chromium steels are reported to have an oxidation resistance similar to that of iron, however, at concentrations greater than 12 at.% Cr and below  $1000^\circ C$  the oxidation resistance is increased almost a hundred-fold [9]. However, oxidation will occur more readily when the Cr content in the matrix falls below the critical value (normally regarded as 12 at.% or 11 wt.% [1]). As discussed

below, a mechanism that reduces Cr content in the matrix, is thought to occur in the material of the present study.

#### 4.2 Mechanisms of oxidation

Oxidation appears to occur preferentially at the scratched sites on the insert and therefore the relationship between this oxide formation and the scratches caused when the insert is assembled into a sleeve is considered.

The oxidation resistance of steel is determined by the composition and thickness of the oxide layer. The existence of Cr oxides will prohibit the contact between iron and oxygen and therefore further oxidation can be prevented. A hard and thick oxide layer with a high Cr content will minimise chemical as well as mechanical oxidation and lengthen the lifetime of components. Auger electron spectroscopy (AES) analysis of the Fe-9Cr-1Mo (wt.%) steel oxidation products has shown that the oxide layer forms a duplex structure consisting of Fe and Cr oxides, and the ratio of these two oxides varies with the oxidation temperature. Below 400°C the oxide layer consists mainly of Fe<sub>2</sub>O<sub>3</sub>, possibly Fe<sub>3</sub>O<sub>4</sub> and a small amount of Cr<sub>2</sub>O<sub>3</sub>. The Cr<sub>2</sub>O<sub>3</sub> oxide layer is reported to thicken as the temperature increases further [10]. In the present study, the virgin inserts were heat treated at 560°C, resulting in the formation of a relatively thick Cr<sub>2</sub>O<sub>3</sub> layer. The observed scratches were produced in the course of fitting the inserts thus damaging the integrity of the initial Cr<sub>2</sub>O<sub>3</sub> oxidation film, and thus allowing the bare alloy to be exposed in the working environment at a temperature of ~ 200°C, in which Fe<sub>3</sub>O<sub>4</sub> and Fe<sub>2</sub>O<sub>3</sub> preferentially form.

Thus the above explanation is consistent with the observation that the oxidation is caused by the scratches which damage the thin oxidation protection layer. Indeed, significant corrosion/oxidation is noted to only occur within the scratches. In addition, for the failed inserts, oxidation was also present around a significant proportion of the outer rim circumference of the inserts, with or without scratches. This phenomenon can be related to a tribocorrosion mechanism in which a combination of oxidation and abrasive wear occurs (i.e. abrasion de-passivates within scratches followed by oxidation of nascent scratch areas in oxygen environment). Oscillation of two metallic surfaces produces tiny metallic fragments that oxidise and become abrasive particles. Subsequent wear proceeds by mild adhesive wear in combination with abrasive wear.

The above oxidation mechanism via assembly scratches and tribocorrosion relies upon the Cr content being lower than 11 wt.%, the amount required to form a continuous film of Cr<sub>2</sub>O<sub>3</sub> with which to prevent the corrosion/oxidation. However, the studied alloy has a nominal Cr content above 11 wt.%, which therefore should still be regarded as stainless. Therefore, possible depletion of the Cr content in the matrix of alloy needs to be considered. A possible mechanism for this is analysed below.

#### 4.3 Mechanisms of failure

The most common mechanism for depletion of the Cr content in the matrix is due to the formation of particles which have a high percentage of Cr. Therefore, the common Cr-rich particles such as carbides ( $\alpha'$ ) and sigma-phase ( $\sigma$ ) will be reviewed, and consideration of whether they could have formed in the present alloy will be made.

##### *Embrittlement at 475 °C by $\alpha'$*

After long-term service in the range of 300-500°C, steels with more than 15% chromium become brittle and lose corrosion/oxidation resistance. This is referred to as 475°C embrittlement because peak hardness on ageing occurs at this temperature. The generally accepted mechanism is due to the precipitation of small spherical particles, ~20 nm in diameter of a chromium rich (80%) bcc phase  $\alpha'$  with a lattice parameter close to that of the matrix  $\alpha$ , first observed by TEM by Fisher et al. [11]. The precipitation of  $\alpha'$  in high purity Fe-Cr alloys can occur by either spinodal decomposition

or by nucleation and growth, depending upon the composition and ageing temperature. However,  $\alpha'$  particles are rarely noted unless the chromium content exceeds 13%. The particles observed in this study are therefore unlikely to be  $\alpha'$ .

### ***Formation of sigma phase ( $\sigma$ )***

The properties of alloys subjected to 475°C embrittlement can be restored by heating above 538°C; however excessive holding may result in sigma-phase ( $\sigma$ ) embrittlement, which in turn can be eliminated by heat treatment above 870°C [13]. Sigma-phase, often described as FeCr, is difficult to form in alloys with less than 20% Cr, but forms readily in alloys with 25–30% Cr when heated between 500–800°C. Elements such as Mo, Si, Ni, and Mn shift the sigma-forming range to lower chromium contents. Sigma-phase consists of a tetragonal unit cell with lattice parameters of  $a = 0.83 - 0.92$  nm,  $c = 0.45 - 0.48$  nm with the variations due to small changes in composition. The unknown phase in this study is not  $\sigma$  phase, as the structure and lattice parameters have been shown to be very different. Laves phase (typical composition for Cr containing steels  $(\text{Fe,Cr})_2(\text{Mo,Nb,Ti,Si})$ ) is another candidate [12], but its reported structure (hexagonal) is very different from the phase observed in the present alloy.

The formation of carbides degrades corrosion/oxidation resistance, and the formation of  $\alpha'$  or  $\sigma$  phase is normally regarded as the reason for embrittlement. These phases are all Cr-rich, which depletes the Cr content in the adjacent matrix and thus causes sensitivity to corrosion/oxidation. As the present observed phase has a high Cr content, it is inevitable that the Cr content in the matrix has been reduced below 11 wt.%, which is regarded as the lowest value to keep a steel stainless. Therefore, once the protected layer is broken down, the reduced Cr content of the matrix will cause a reduced resistance to oxidation and the high service pressures can induce brittle fracture at the thinner sections of the insert, i.e. the rim of the insert.

### ***Carbides***

Other reported Cr-rich phases, however, such as Laves ( $\eta$ ), Chi ( $\chi$ ), R, and Tau ( $\tau$ ) could be responsible for the reduction in Cr content of the matrix. However, none of these possess the fcc structure [12]. Three carbides are commonly observed in the present steel:  $\text{M}_7\text{C}_3$ ,  $\text{M}_{23}\text{C}_6$ ,  $\text{M}_6\text{C}$  [12,13].  $\text{M}_7\text{C}_3$  is present at tempering temperatures of approximately 480°C.  $\text{M}_{23}\text{C}_6$  becomes the predominant carbide at 540°C and above.  $\text{M}_7\text{C}_3$  seriously degrades corrosion resistance, as its presence depletes the chromium content in the matrix adjacent to Cr-rich particles. In this study, an fcc phase of  $a = 1.07 \pm 0.03$  nm with Cr rich compositions detected with a carbon content from 13–20 at.%. It is therefore considered to be as carbides. The only fcc structure in carbides is  $\text{M}_{23}\text{C}_6$  or  $\text{M}_6\text{C}$  with carbide contents of 20.6 at.% and 14 at.%, respectively. It is hard to distinguish these two particles from EDS results as EDS measurement for light elements are always unstable. The further structure determination for this phase as  $\text{Fm}\bar{3}m$  exclude the  $\text{M}_6\text{C}$  which has  $\text{Fd}\bar{3}m$  structure. Therefore they are thought to be  $(\text{Cr,Fe,Mo})_{23}\text{C}_6$  carbides. These precipitates are preferably observed in the grain boundaries of austenite matrix [1], but in this study they seem to distribute within the grain. It is perhaps due to the martensite / ferrite matrix.

In fact, the precipitates could be as small as 10 – 20 nm in oil quenched samples as shown in Fig. 7(a). These precipitates will grow up to 50 nm after heating 560°C for 3h (Fig. 7b). Further SEM analysis of samples subjected to additional heat treatments show that precipitation depends on the cooling rate; the faster the cooling rate, the larger the precipitates that form. The precipitates could be avoided at slow cooling speeds, such as air-cooling (Fig. 8) although they might be formed in the further heat treatment.

The present investigation thus indicates that the poor oxidation resistance performance of this alloy results from the formation of Cr rich  $(\text{Cr,Fe,Mo})_{23}\text{C}_6$  precipitates which deplete the Cr content in the matrix.

## 5. Conclusions

An insert made from Jethete M152 type stainless steel, which failed in service, was investigated using scanning and transmission electron microscopy. A high density of Cr-rich precipitates has been observed by SEM. TEM analysis indicates that this is a  $(\text{Cr,Fe,Mo})_{23}\text{C}_6$  carbides which possess a  $\sqrt{3}m$  structure with a lattice parameter of  $1.07 \pm 0.03$  nm. The premature failure of these inserts is due to the formation of these Cr-rich precipitates, which deplete the Cr in the adjacent matrix, and in turn reduce the oxidation resistance and induce embrittlement. This oxidation, in combination with subsequent abrasive and adhesive wear, led to the premature failure as a result of tribocorrosion.

## Acknowledgements

The helpful technical discussions with Patrick Young are gratefully acknowledged

## References

- 1 Davies JR (Ed). Stainless steels, ASM Specialty Handbook, ASM International, Ohio, 1994.
- 2 Davies MH, Mehl RF, Birchenall CE. J Metals 1951;3:889.
- 3 Buxton BF, Eades JA, Steeds JW, Rackham GM. Philos Trans R Soc London ser A1976;281:171-94.
- 4 Steeds JW, Vincent R. J Appl Cryst 1983;16:317-24.
- 5 Steeds JW. In: Hren JJ, Goldstein JI, Joy DC eds., Introduction to Analysis Electron Microscopy, New York: Plenum Press, 1979:387
- 6 Wright IG. High-Temperature Corrosion, Corrosion, Vol. 13, ASM Handbook, ASM International, 4<sup>th</sup> ed. 1992, p.97-101.
- 7 Lai GY. in: High-Temperature Corrosion of Engineering Alloys, ASM International, 1990.
- 8 Richardson FD, Jeffes EJ. Iron Steel Inst 1948;160:261.
- 9 Shrier LL, Jarman RA, Burstein GT (Eds). Corrosion, 3<sup>rd</sup> ed, Butterworth-Heinemann, Oxford, 1994.
- 10 Greeff AP, Louw CW, Swart HC. Corros Sci 2000;42:1725-40.
- 11 Fisher RM, Dulis EJ, Carroll KG. Trans AIME 1953;197:690.
- 12 San Martin D, Rivera Diaz del Castillo PEJ, Peekstok E, van der Zwaag S. Mater Character 2007;58:455-60.
- 13 Peckner D, Bernstein IM (Ed.), "Handbook of stainless steels", New York : McGraw-Hill, 1977.

Figures



**Fig. 1:** A photograph of a failed insert after service.

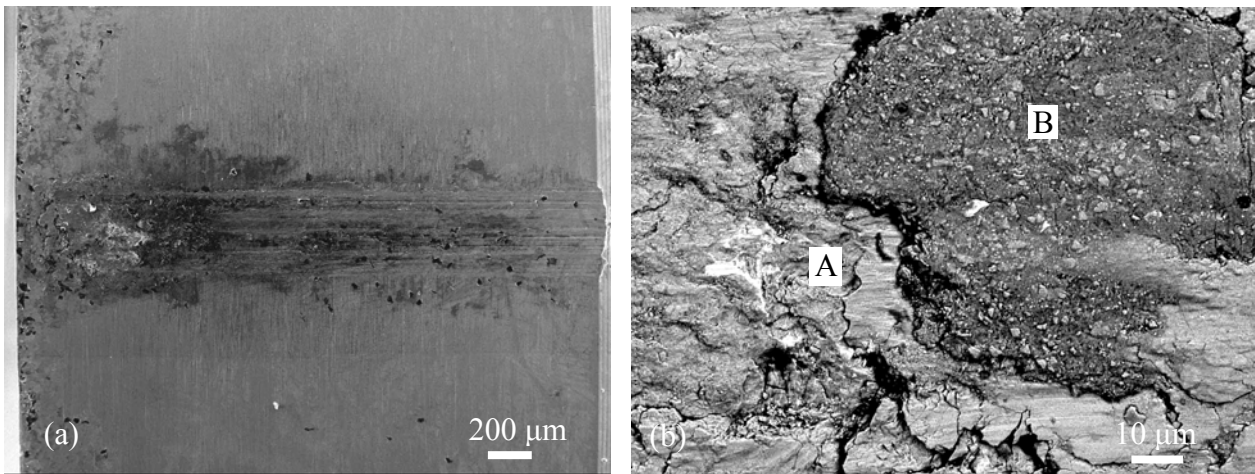


**Fig. 2.** SEM micrographs of area 1 of Fig.1 on the insert. **(a)** SEI at low magnification; **(b)** BEI at higher magnification.

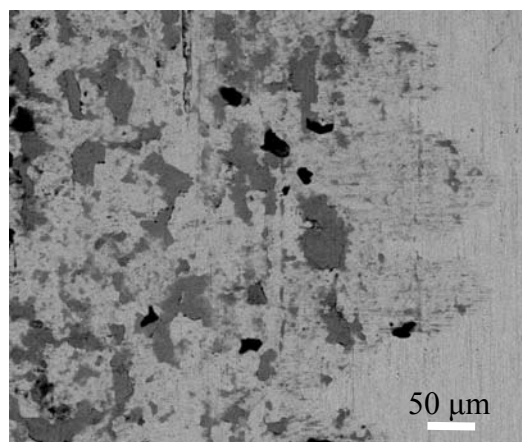


**Fig. 3.** BEI micrograph of area 2 of Fig.1

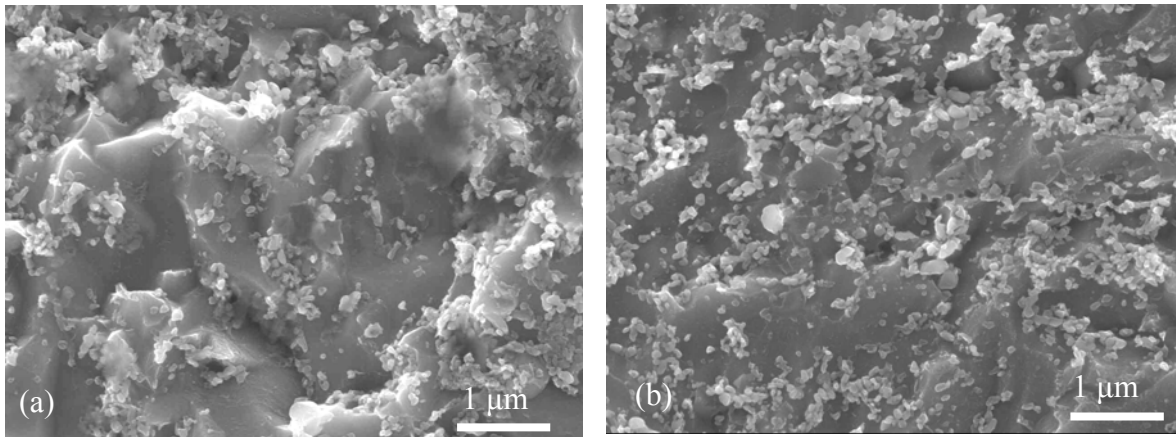


**Fig. 4.** SEI micrographs from the centre of the transverse sections (a) insert that failed in service; (b) virgin insert (prior to service).

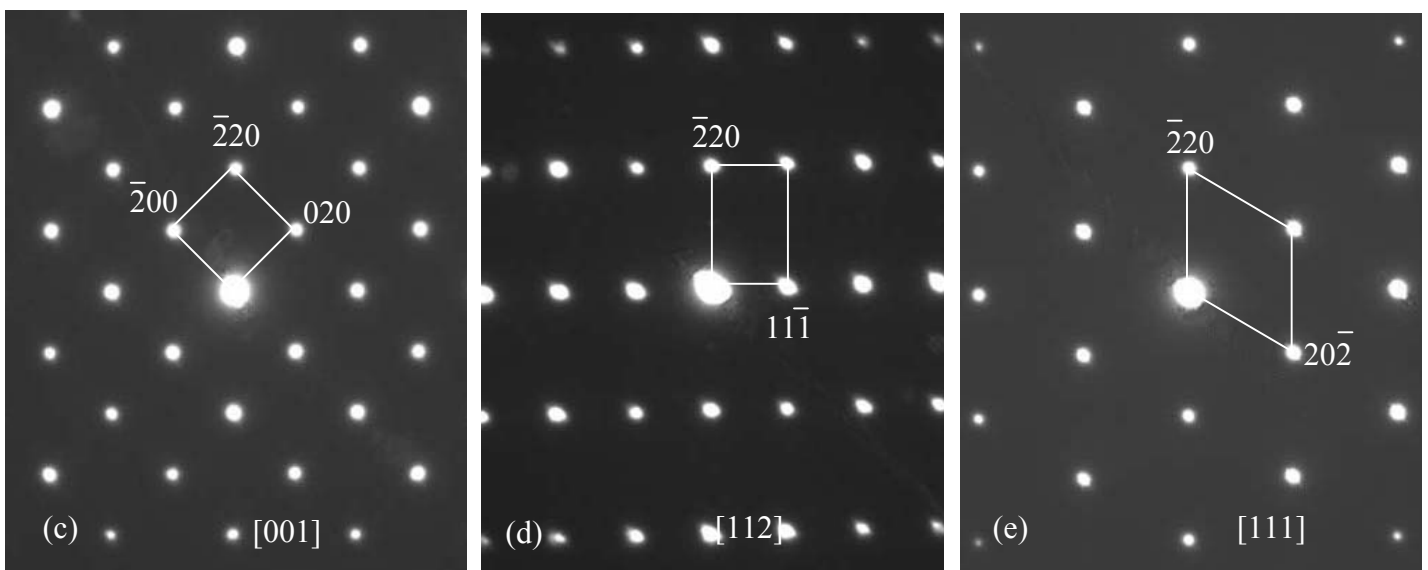
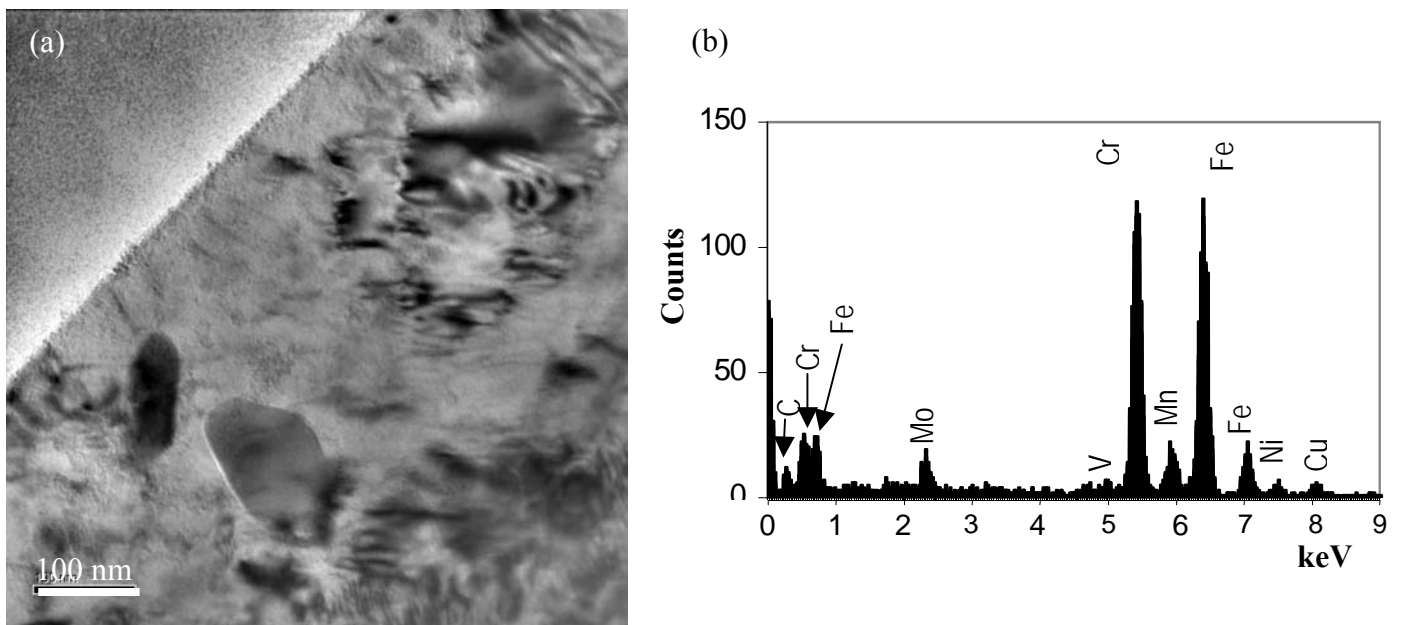


**Fig. 5.** TEM bright field image and the selected area diffraction pattern from the precipitates. (a) bright field image; (b) EDS analysis of the precipitate (c-e) [001], [112] and [111] diffraction patterns of the precipitate, respectively.

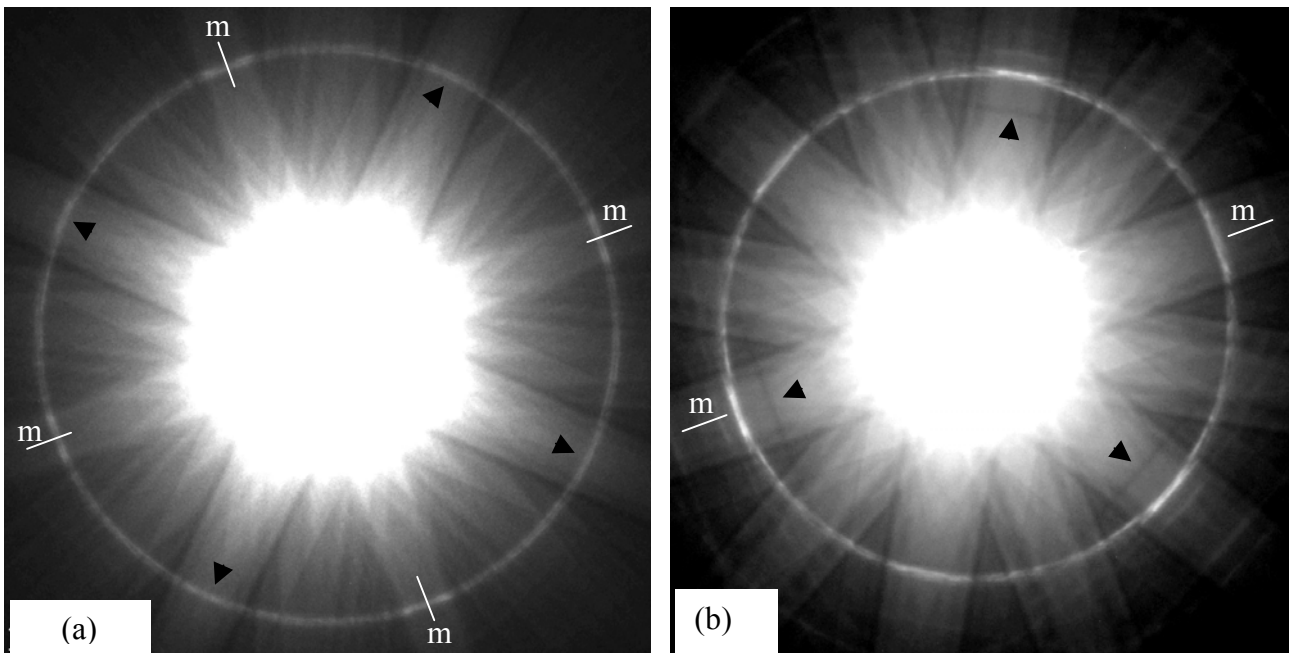


**Fig. 6.** Convergent beam electron diffraction patterns of (a) [001] and (b) [111] zones, which are corresponding to the SAD patterns of Figs. 5(c) and 5(e), respectively. m represents a mirror symmetry.

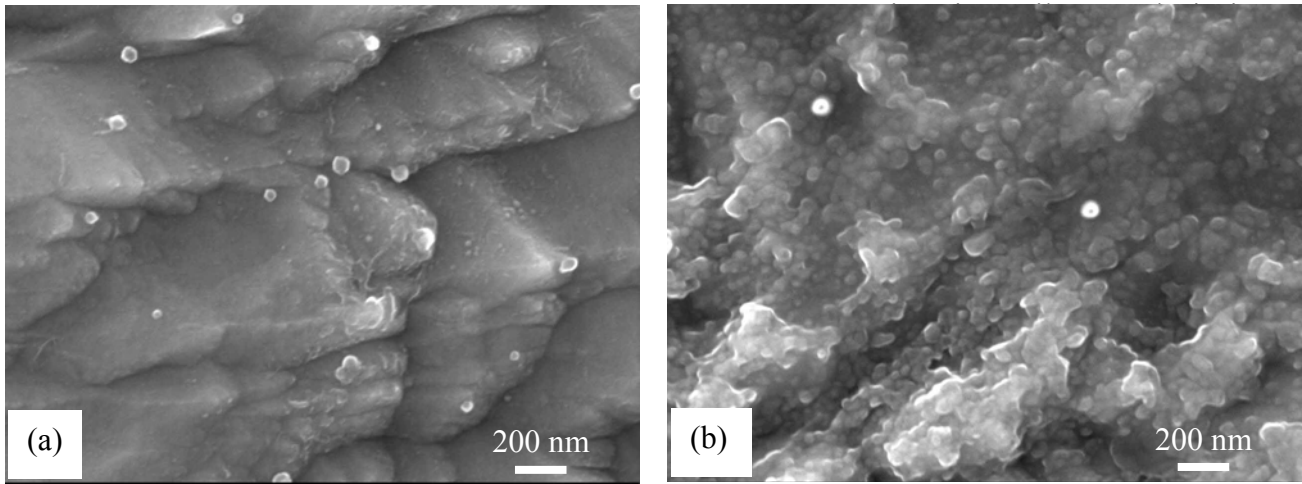


Fig. 7. SEI micrographs of one insert after (a) solution treatment at 1050°C for 1 h, oil quenched and (b) further heat treatment at 560°C for 3 h.

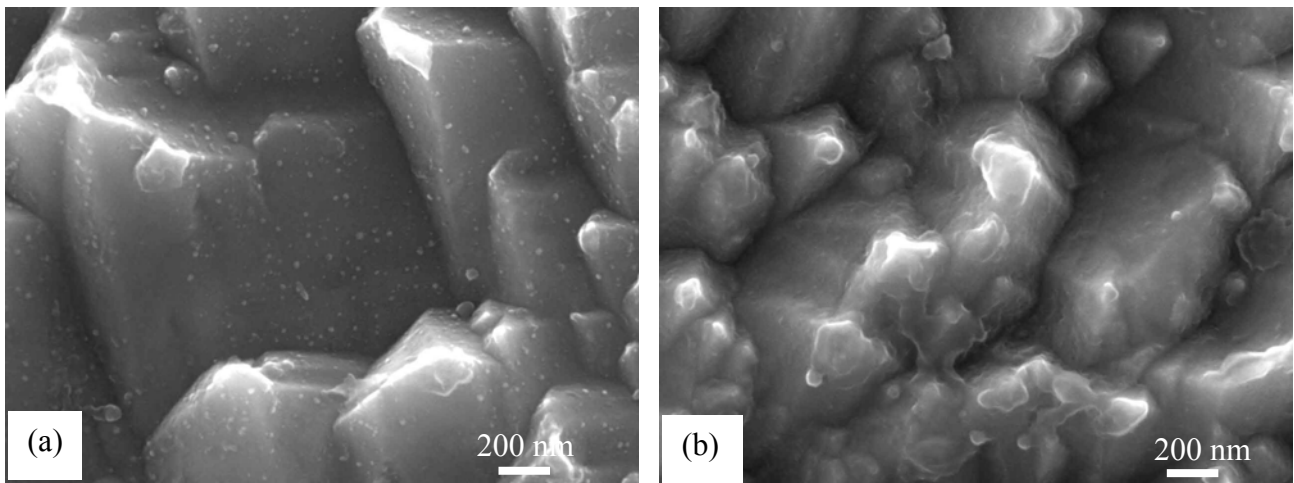


Fig. 8. SEI micrographs of one insert after (a) solution treatment at 1050°C for 1 h, and subsequent water quenching and (b) air cooling.